



Experimental and numerical investigation of an arch–beam joint for an arch bridge

Yan Yang^{1,2} · Benqing Lin¹ · Wei Zhang^{1,3}

Received: 29 December 2022 / Revised: 7 March 2023 / Accepted: 19 March 2023 / Published online: 25 March 2023
© Wrocław University of Science and Technology 2023

Abstract

In this paper, the stress analysis of the most critical beam–arch joint of Yuehu Bridge is conducted, despite the variation in the specific structure of each tied arch bridge. To achieve this, two specimens with different scale ratios were designed. The smaller specimen was used to consider the effect of bridge deck and loading to failure. The experimental results indicate that both specimens did not exhibit significant deformation under the design load, and the measuring point's stress was located in the elastic section. This implies that the original bridge structure design is rational. However, the arch rib steel plate of the 1/8 scale specimen buckled when subjected to 1.8 times the design load. To validate the experimental results, a finite element model that considers the elastoplastic behavior of the material was established and compared with the experimental results. The comparison shows that the finite element model can predict the mechanical behavior of the structure effectively, thus confirming the rationality of the structure design. Additionally, the study also analyzed the buckling problem of tied arch bridges, which is another critical issue. The in-plane and out-of-plane buckling of fixed and hinged parabolic arches under uniform axial compression were investigated. The results demonstrate that the boundary conditions, rise-span ratio, and bridge deck width significantly affect the buckling performance. Overall, this study provides essential insights into the stress and buckling behavior of tied arch bridges, which can guide the design and construction of such structures in the future.

Keywords Beam-arch joint · Arch · Mechanical behavior · Finite element method · Experiment

1 Introduction

Arch bridges are widely used and continually updated due to their advantages in reliability, economics, and aesthetics [1, 2]. In recent years, there has been an increasing trend of using arch bridges in urban bridge construction, such as the Lupu Bridge [3], the Xinguang Bridge [4], and the Harbour Bridge in Sydney [5]. The arch–beam bridge is a structure that connects the two ends of the arch with the longitudinal girders of the bridge deck. It is prestressed with an inward horizontal pressure to the arch rib, which proactively balances the thrust. Externally, the bridge is supported under

the same conditions as a girder bridge, with the bearings producing only vertical reaction forces and no horizontal thrust [6]. Internally, most of the internal forces generated by the load in the arch and girder are transformed into the forces of the self-balancing system formed between them. Specifically, the bridge bending moment is transformed into the arch under compression and the main girder under tension, while the shear force is mainly borne by the vertical component of the axial arch force (Fig. 1). Overall, the arch–beam bridge's unique design provides a balance between form and function, making it a popular choice in bridge construction. As such, it is important to continue studying and improving the design and construction of arch bridges to ensure their continued reliability and efficiency.

It is evident that the stress situation at the foot of the arch is complex under the given force conditions. From a construction perspective, the foot of the arch is a critical component that connects the arch rib, the main beam, and the crossbeam. Its construction form is intricate and complex. In terms of force, the foot of the arch is a critical location for bearing the axial force of the arch ribs, the bending moment of the main beam, and

✉ Wei Zhang
Zhangwei621@gmail.com

¹ College of Civil Engineering, Fuzhou University, Fuzhou 350118, China

² Fuzhou University ZhiCheng College, Fuzhou 350001, China

³ College of Civil Engineering, Fujian University of Technology, Fuzhou 350118, China

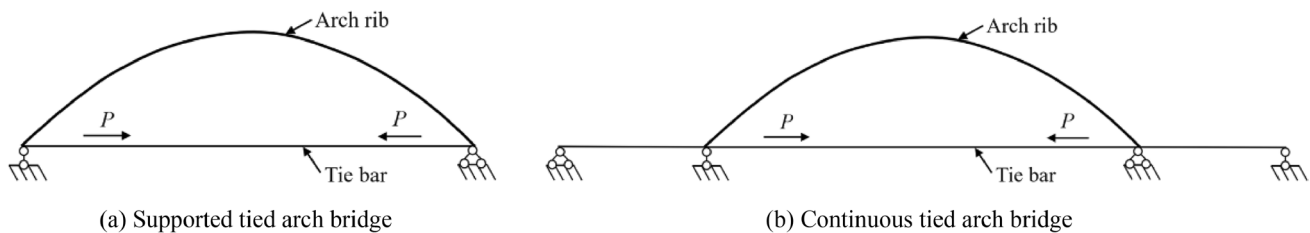


Fig. 1 Structure style of tied arch bridges

the reaction force of the support. Conventional design methods cannot accurately calculate the stresses at this location. In recent years, several studies have investigated the mechanical behavior of arch–beam bridges. These studies aim to provide a better understanding of the complex stress situation at the foot of the arch and to develop improved design methods to ensure the safety and reliability of such structures. Overall, the investigations into the mechanical behavior of arch–beam bridges are essential for advancing the design and construction of these structures. The findings of these studies can guide the development of new and improved design methods that accurately account for the stresses and forces at critical locations, such as the foot of the arch, to ensure the safety and reliability of these structures. In the field of bridge engineering, several studies have investigated the stability and behavior of different arch bridge structures using numerical and experimental methods. For instance, Feng et al. [7] utilized numerical and experimental methods to explore the stability of the steel box arch segment of the Lupu Bridge in Shanghai, China. The primary objective of the scaled test was to investigate the mechanism and stability of the plates. Additionally, local stability analysis was carried out, which was found to be crucial for obtaining reliable results. Similarly, Zhang et al. [8] studied the behavior of a concrete-filled steel tube (CFST) tied arch bridge based on the Maocaojie Bridge in Hunan Province, China. They designed a 1/20-scaled specimen to ensure construction safety and compared the simulated results with the field-measured data to verify their reliability. Moreover, Liu et al. [9] conducted a study on the stability of tied arch bridges using the Bac De Roda Bridge in Barcelona as a reference. They designed five scaled specimens with different arch rib structures to investigate stability. The test results revealed that the use of stabilizing arches can increase the stability and ultimate capacity of tied arch bridges. These studies demonstrate the importance of using both experimental and numerical methods to investigate the stability and behavior of arch bridges. They also highlight the significance of scaling down specimens to ensure safety and reliability in testing. The findings of such studies can provide valuable insights for improving the design and construction of arch bridges.

Since arch bridges are pressure-dominated structures, buckling problems under pressure may lead to overall structural instability. Therefore, buckling analysis is one of the

essential processes when performing design calculations for steel bridges. With the development of finite element technology, the FE model method has become a standard method for buckling analysis. Poutré et al. [10] studied the elastic–plastic out-of-plane buckling response of I-section arches by series of experimental tests. Totally, 15 specimens were tested under measuring the geometric imperfections. It was observed that all arches' failed reasons were elastic–plastic out-of-plane buckling. Wei et al. [11] proposed a nonlinearity finite element program to investigate the characteristics of parabolic fixed steel tubular arches under critical loads. The proposed program can involve the geometric and material dual nonlinearity. Comparing the various experimental test results shows that remarkable capability of proposed program to predict the in-plane critical load of parabolic fixed steel arch. Guo et al. [12], Lu et al. [13], and Huang et al. [14] performed the experimental analysis to study the elastic–plastic buckling of steel arches. Of course, the fatigue problem is also one of the important research directions of tied arch bridge. For example, Professor D'Amato et al. [15–17] have conducted in-depth research on this aspect. However, due to the purpose of the test and the limit of the length of the paper, this paper does not carry out relevant fatigue performance research.

In the present work, two beam–arch joint specimens were performed, and their mechanical behavior was studied by experimental and numerical investigations. The framework of this paper is as follows. In Sect. 2, the experimental program of the beam–arch joint is introduced. Section 3 examines the strain and stress of the measurement points on the beam–arch joint analytically and experimentally. Section 4 analyzes the buckling strength of the Yuehu Bridge. Section 5 gives the conclusions lastly (Fig. 2).

2 Experimental program

2.1 Specimen design

It is essential to perform extensive research to investigate arch bridges' mechanical and dynamical behavior and develop the bridge's associated safety and serviceability—Yuehu Bridge, which is in Yingtang city of Jiangxi province

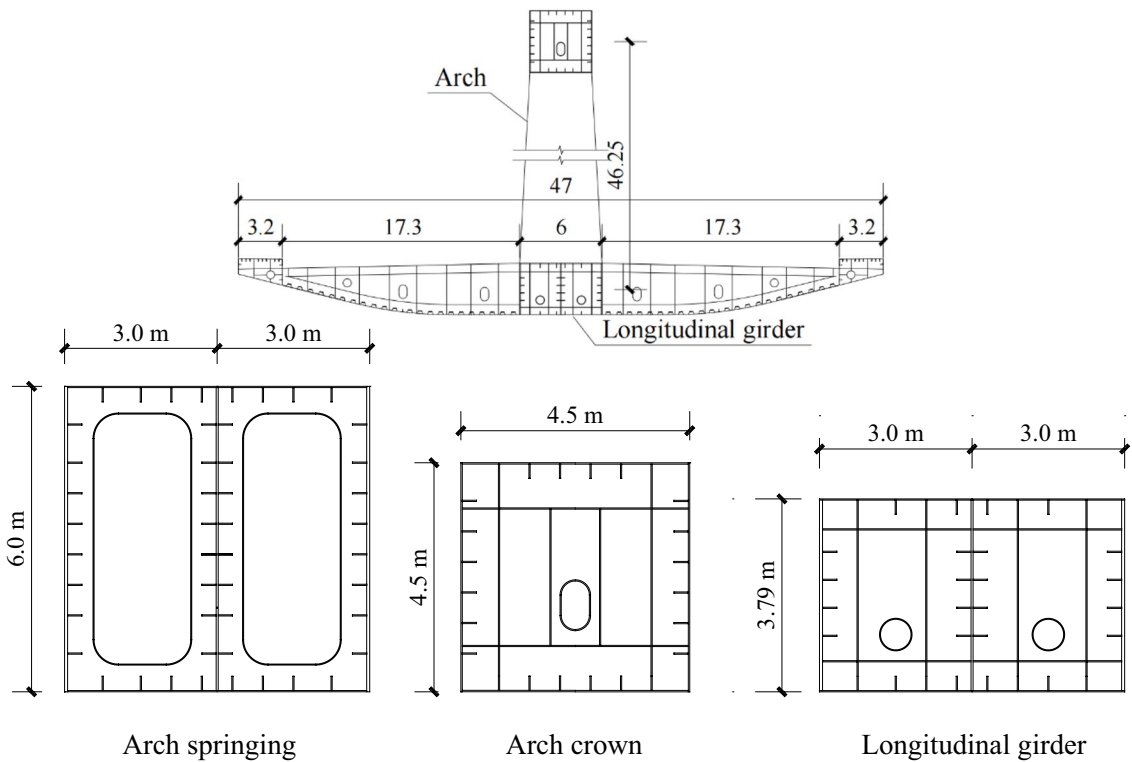
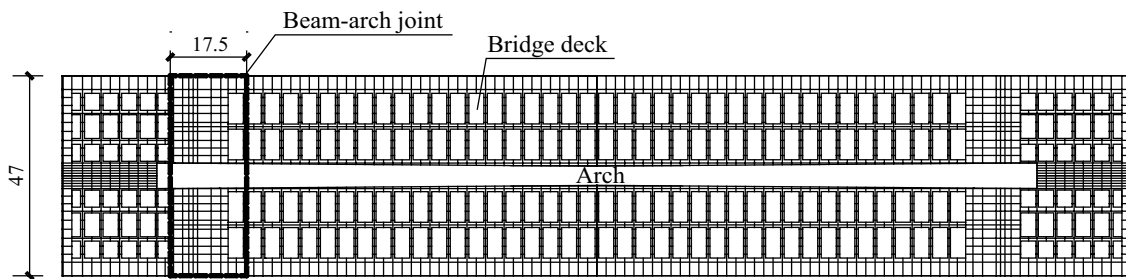
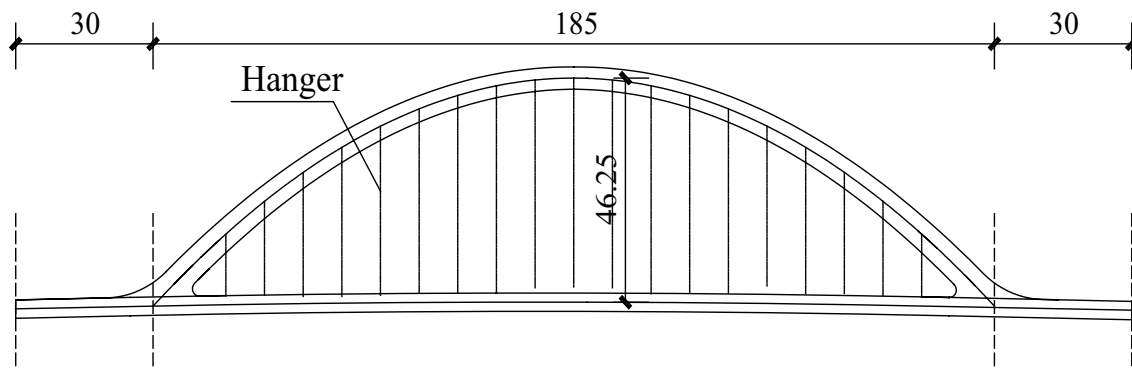


Fig. 2 General arrangement of Yuehu Bridge (unite: m)

in China. The bridge's total length is 245 m, the main arch span is 185 m, and the rise-to-span is 1/4. The bridge was constructed using a girder followed by an arch construction scheme. The main girders were erected in the same way as conventional steel girder bridges, and the arch ribs were welded in sections with brackets erected on top of them after the main girders had been erected. To increase the integrity of the beam–arch joint, the section of the arch rib near the arch foot is subsumed in the erection of the main girder. To increase the stiffness of the end of the arch rib, a double box section is used near the foot of the arch, while a single box section is used at the remaining locations. The beams and arches are completely rigidly connected at the foot of the arch, where the arch ribs, main beams, and crossbeams intersect in a complex stress state, and there is no relevant design code as a reference. Therefore, an experimental test is necessary further to understand the mechanical behavior of the beam–arch joint.

Two specimens of the beam–arch joint were designed, which were named W-1 and W-2, respectively. Table 1 shows the two specimens' model scale, length, width, height, and weight. The scope of the specimen is intercepted according to the original segmental construction scheme of Yuehu Bridge. The area size of the beam–arch joint is exactly the same as that of the W-1 specimen, while the W-2 specimen is intercepted according to the zero point of the transverse bending moment, the transverse interception section is only axial force and shear force. At the same time, the extension of the arch rib section of the W-2 specimen is to analyze the stress of the single box transfer multi-box.

To investigate the difference between the W-1 and W-2 specimens, the interception ranges of the two specimens are compared, as shown in Fig. 3. To clarify the force transfer process between single and multiple boxes, the W-2 specimen has an extension of arch rib on the front view; because of the whole section on transverse direction, the specimen W-1 has two extension sections on plan view.

The model scale of W-1 and W-2 specimens were 1:8 and 1:5, respectively. Table 2 lists the similarity ratios of the specimens to the real bridge. Since the similarity ratio of stresses is 1, the stresses of the model are the same as those of the real bridge. Table 3 shows the mechanical properties of steel; the model and prototype are both Q345qD steel.

The specimens were fabricated procedures as following:

Step 1: Welding construction platform according to the radian of the bottom plate, as presented in Fig. 4a.

Step 2: Processing parts and placing them in categories, as presented in Fig. 4b, c.

Step 3: Welding the component from the bottom to the top and arranging its internal strain gauges during the process, as presented in Fig. 4d, e.

Step 4: Encapsulate the top plate and welding the parts for hoisting, as presented in Fig. 4f.

2.2 Loading device

The entire load, except for the load associated with the bridge counterweight, was applied by hydraulic jacks, and the forces' values were monitored by load cells. Figure 5 presents sketches of the loading device of specimens. The axial force and bending moment acting on the arch rib were applied by a 6000-kN jack named 1#jack. The axial and shear forces on the boundary section of the beam were applied using two 1000 kN jacks named 2#jack and 3#jack, respectively. The shear forces on the cross-bridge direction were applied using 300 kN jacks named 4#jack and 5#jack.

2.3 Test scheme

Measuring the strains under the worst-case loads is the test's primary purpose. Therefore, there are 192 strain measuring points on the two specimens.

The measuring points for the beam–arch joint were divided into two parts: the arch and the beam. There were five test sections on the arch labeled from I to V. In addition, the test sections on the beam were labeled A to E, as shown in Fig. 6. In the figure, the strains arrangement on each test section was illustrated, there were 12 test points on the A–E test sections, and there were 4 test points on the I–V' sections.

2.4 Loading cases

Three loading cases were studied for different testing purposes in order to further explore the static performance of the beam–arch joint, as outlined in Table 4. The three loading cases were described in detail as follows:

Case 1: The objective of this case was to investigate the strength of the beam–arch joint by testing the critical parameter stresses of the W-1 specimen with the live load arrangement in the negative bending moment influence line of the bridge.

Case 2: The purpose of this case was to further investigate the static behavior of the bridge and test its limit load-carrying capacity. This is because the beam–arch joint is a vital force transmission component of the arch bridge. In this case, overloads with 1.8 times the load of Case 1 were applied to the W-1 specimen.

Table 1 Details of specimens

No.	Model scale	Length (m)	Width (m)	Height (m)	Weight (t)
W-1	1/8	2.2	5.1	1.4	2.8
W-2	1/5	3.5	3.3	2.3	7.8

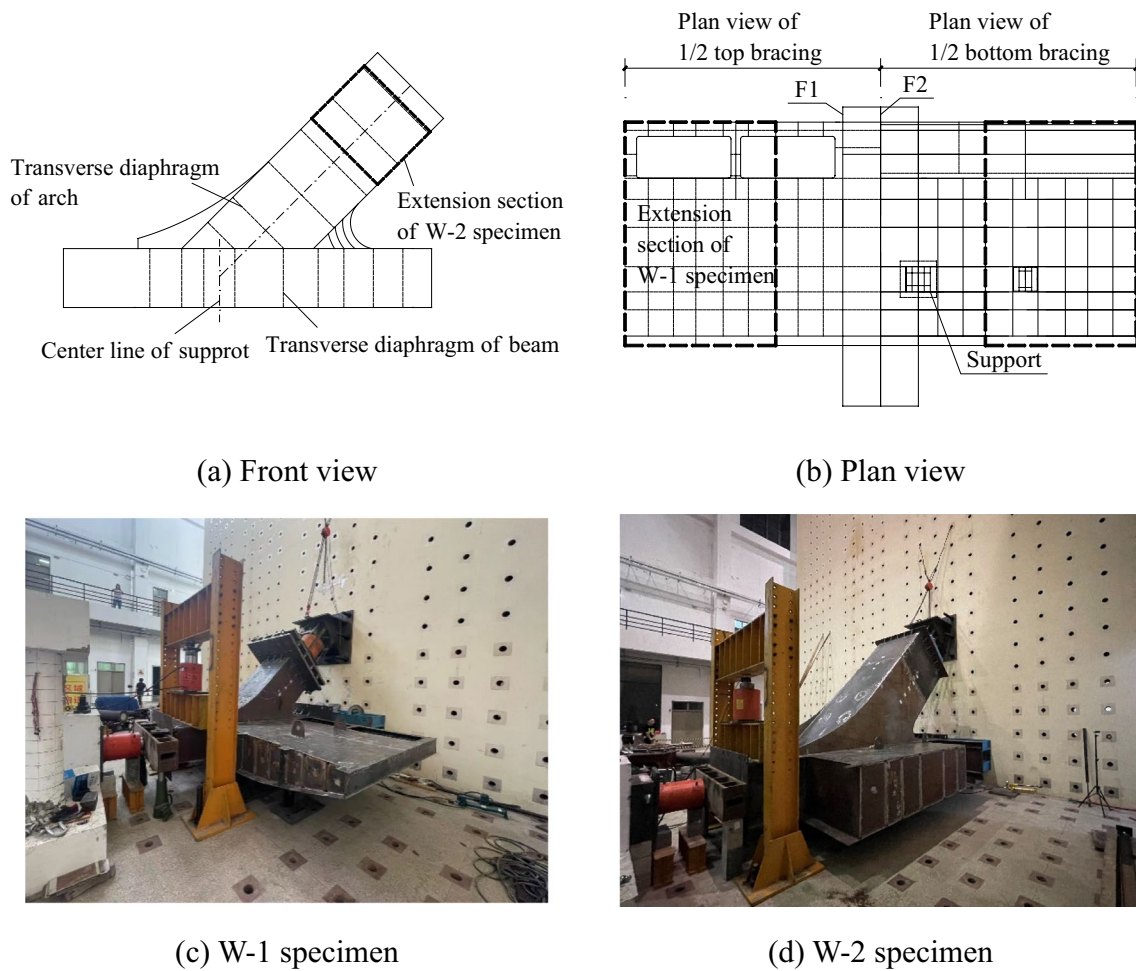


Fig. 3 Sketch of the beam-arch joint specimens

Table 2 Similar ratios of the specimen to the prototype

Parameter	Similar ratios	Similar ratios
Geometrical dimension	1:5	1:8
Concentrated load	1:25	1:64
Moment	1:125	1:512
Density	1:1	1:1
Young's modulus	1:1	1:1
Stress	1:1	1:1
Strain	1:1	1:1

Table 3 Mechanical properties of Q345 steel

Young's modulus (MPa)	Yield strength (MPa)	Tensile strength (MPa)
2.02×10^5	469	579

Case 3: The aim of this case was to estimate the force performance of the junction of the arch rib box on the W-2 specimen, with the worst-case load of axial force of the arch rib.

The test was carried out in three steps in total by linear loading. According to the arch bridge analysis under the worst-case load, the Values of the applied loads are determined. The load magnitude of the specific steps is shown in Fig. 7.

3 Test result and discussion

3.1 Failure mode

Figure 8 illustrates the deformation of the W-1 specimen under final failure conditions. During the initial loading stage, no phenomena occurred on the specimen. The

Fig. 4 Specimens manufactured process



deformation of the arch rib appeared at 1.5 times the design load. With the gradual loading of the load up to 1.8 times the design load, the deformation range increased, the expansion height increased, and failure phenomena appeared on other surfaces of the arch rib. Under the failure load, the buckling position's length, width, and height were 750 mm, 400 mm, and 36 mm, respectively. It can be observed that when the specimen was damaged, there was no obvious deformation except for the arch rib. The final failure was a local buckling failure.

The analysis of the damage mode shows that there are two main reasons for this damaging phenomenon: (1) the downward eccentric design bending moment caused the axial force to be applied off-center; (2) at the 1:8 scale reduction, the spacing between the internal cross-partitions of the complex beam–arch consolidation joint was drastically reduced, leaving less space for welding construction inside. As a result, the webs and top plates at the bulge of the arch ribs were not welded during the processing of the specimen.

3.2 Load–strain curves

One of the critical objectives of the test was to analyze the mechanical behavior of the beam–arch joint under the limited state load of the load-carrying capacity. The load–strain curves for Sections C, D, and III (III') of W-1 and W-2 are presented in Figs. 9 and 10. It can be observed from these figures that the load–strain at the measured points is almost linear before reaching 100% load ratio, indicating that the material is still in the linear elastic phase. As the load continues to increase up to 180% load ratio, the strain of the arch rib measuring point undergoes a mutation, which is caused by local buckling of the steel plate, as shown in Fig. 9c.

3.3 Finite element analysis

The three-dimensional (3D) shell elements S4R of ABAQUS were used for modeling, with each element having five degrees of freedom (DOF) at each node: three translational and two rotational. Figure 11 shows the finite element model

Fig. 5 Sketch of the loading device

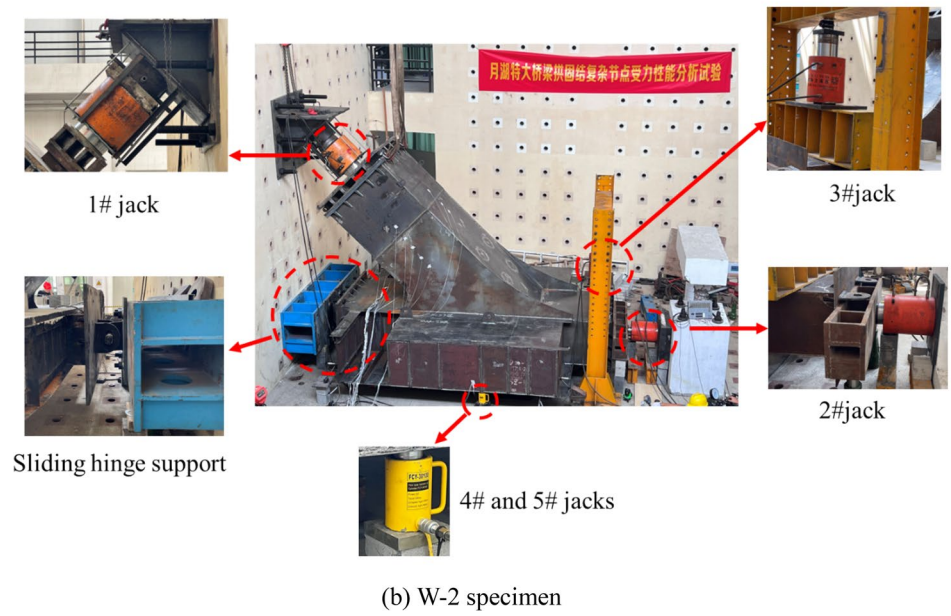
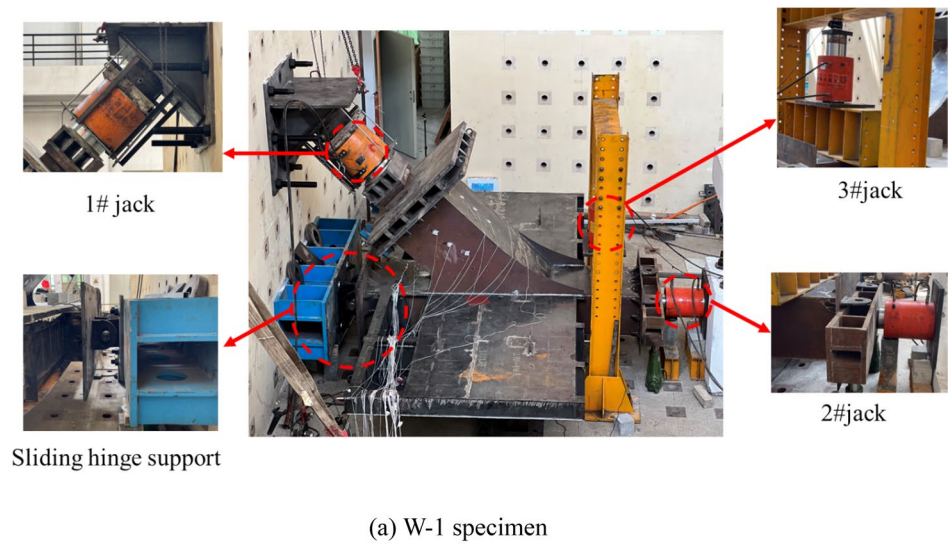


Fig. 6 Locations of sections for strain measuring

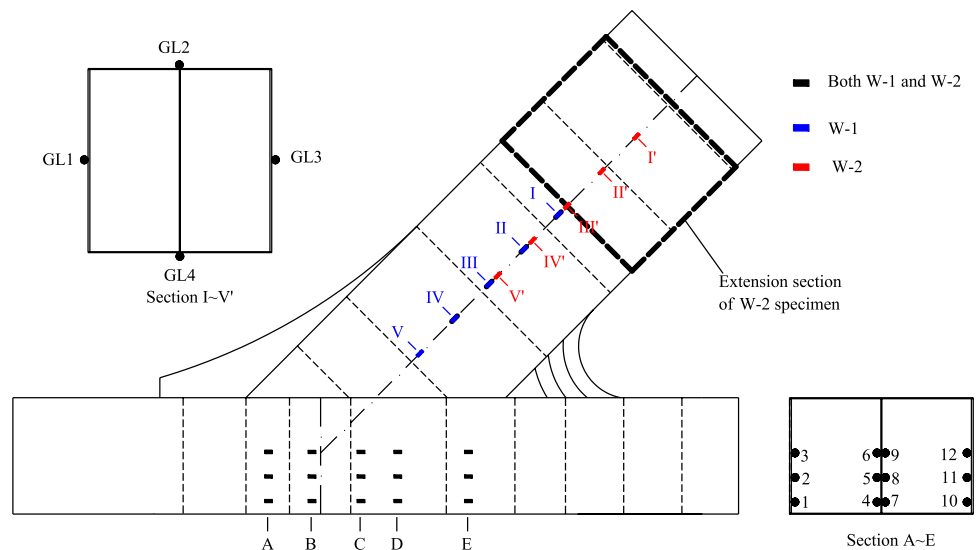


Table 4 Load cases

Case number	Load description	Specimen
1	Strength of the beam–arch joint	W-1
2	Performance of the junction of the arch rib	W-1
3	Limit load-carrying capacity	W-2

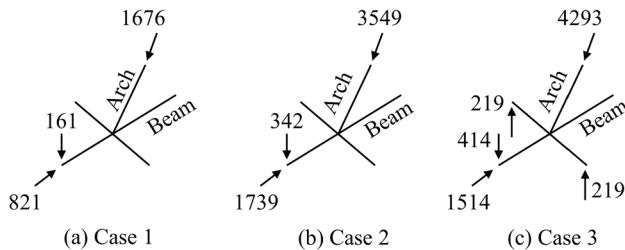


Fig. 7 Load applied on difference cases (unit: kN)

of the specimen, which was established using 210,474 shell elements and 202,844 nodes, after carefully studying mesh convergence and determining an appropriate mesh density.

The purpose of this test was to verify the stress conditions of the beam–arch joint under design loads. The stress results during the worst loading case are shown in Fig. 12, with the maximum compressive stress being 181 MPa and the ultimate tensile stress being 96 MPa. Therefore, the maximum stresses are less than the yield strength (345 MPa), indicating that the beam–arch joint can meet the requirements and is sufficiently safe.

3.4 Comparative study of model test and FEA result

Figure 13 shows the results of the experiments compared with the finite element analysis under the worst-case loading. The experimental results are similar to the simulation results from the aspects of stress and the curve shape, and the difference between experimental and simulated results is mostly within 20%.

From Fig. 13, it can be observed that the maximum tensile and compressive stresses for a 100% load ratio are 63 MPa

and 194 MPa, respectively. This satisfies the requirement that the allowable stress and yield strength of Q345qD must be less than 305 MPa and 345 MPa, respectively, as per GB 50017-2017 [18]. Therefore, the design of the beam–arch joint is safe and reliable. Under the 180% load ratio, the first principal stress of section IV of the arch changes from compression to tensile due to the steel bulging. However, the axial stresses of the other test sections are less than the yield strength.

Figure 14 shows the maximum principal stress curve of the W-2 specimen. It is evident that the measured stresses of the tested model are very close to those of FEA results. The axial stress variation law of the beam on the W-2 specimen is similar to that on the W-1 specimen since the measurement points of the two components are arranged in the same position. However, the two specimens were studied for different purposes, resulting in different axial strain distribution patterns for the arch due to other measurement point arrangements.

3.5 Analysis of the force transmission mechanism

The primary research objective of the W-2 member was to analyze the law of force transfer between single and multiple boxes. Figure 15 illustrates the structure of the chamber change, while Fig. 16 shows the detailed distribution of principal stresses on the transition section of the box girder. It can be observed from the figure that the stress concentration phenomenon of the axial stress of the arch rib at the change of the box chamber is mainly due to the change in stiffness at this location.

The main beam is a critical structure for transferring the internal force of the arch to the bearing. Figure 17 illustrates the stress distribution of the axial stress of the main beam in the 100% load proportional state for the W-1 and W-2 members. It can be observed from the figure that, due to the influence of the axial force of the arch ribs, there are significant gradients in the axial direction of the C and D sections in the vertical main beam direction.

Fig. 8 Failure mode of W-1 specimen

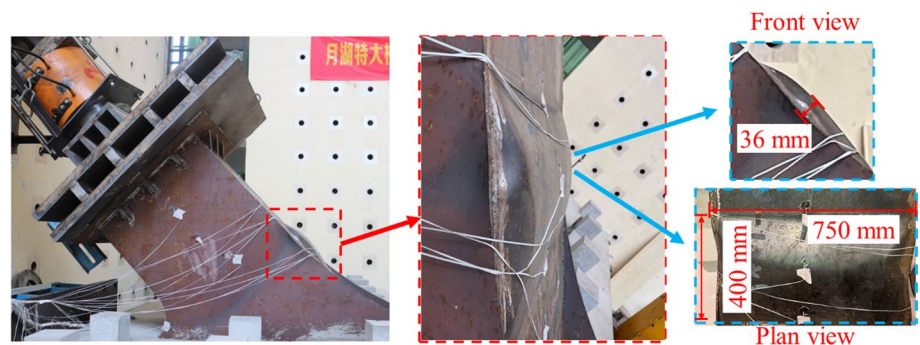


Fig. 9 Principal strain–load curve on W-1 specimen

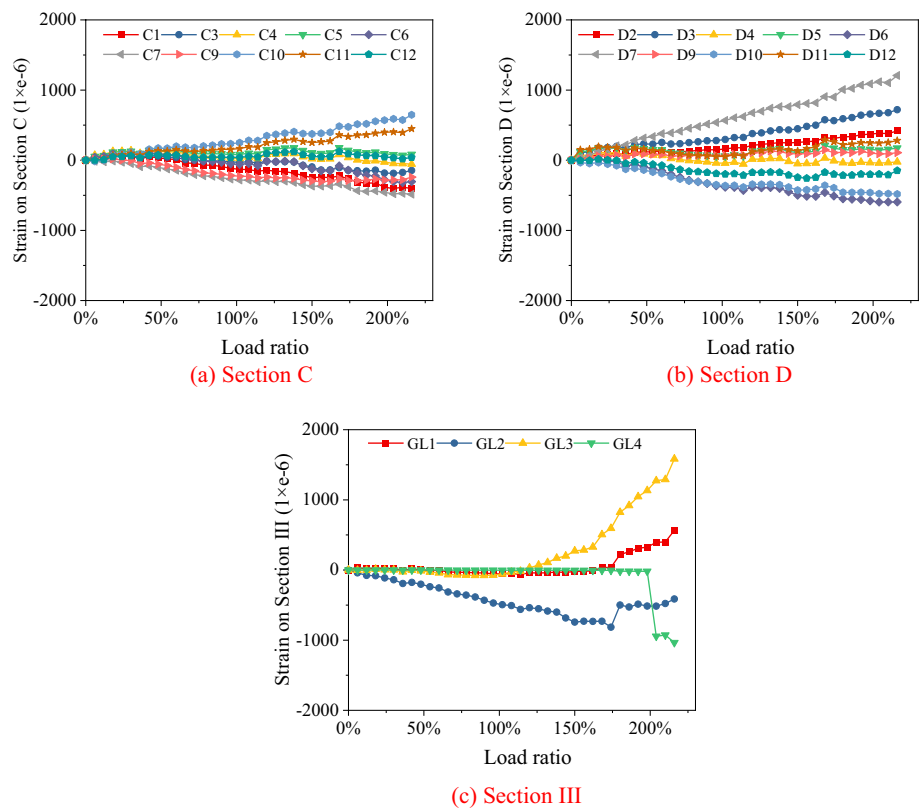
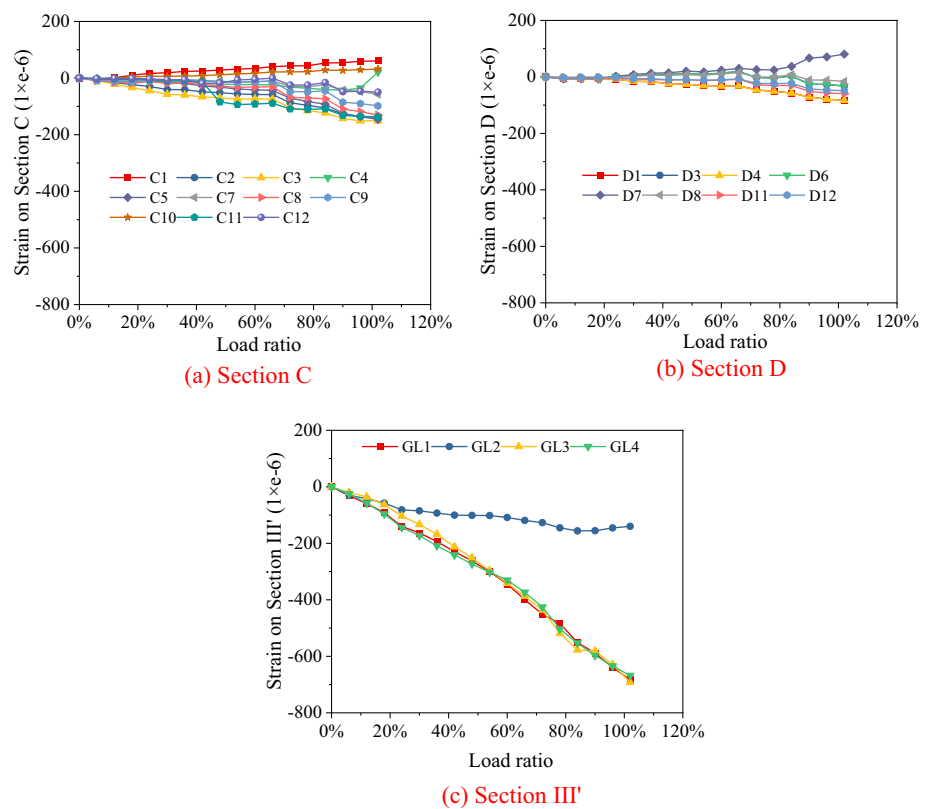


Fig. 10 Principal strain–load curve on W-2 specimen



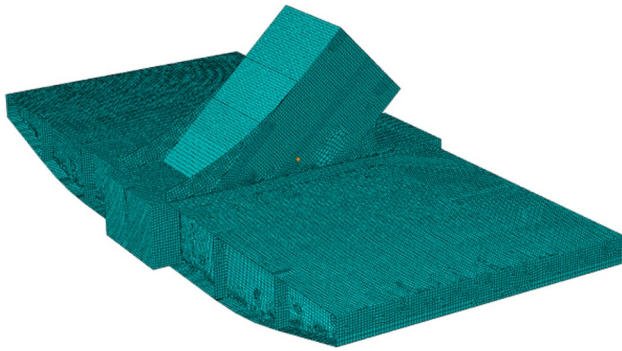


Fig. 11 Three-dimensional FE model

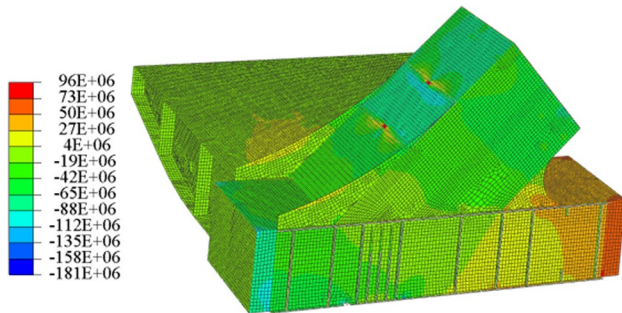


Fig. 12 Normal stress in the axial direction (unite: Pa)

Fig. 13 The maximum principal stress curve on the W-1 specimen

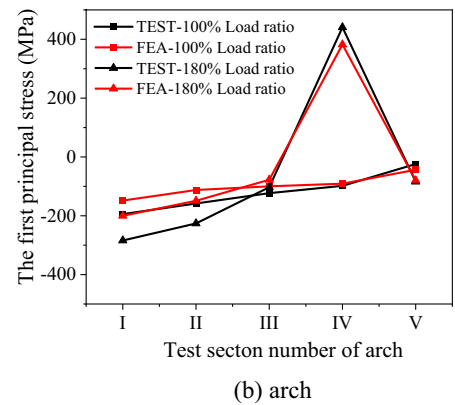
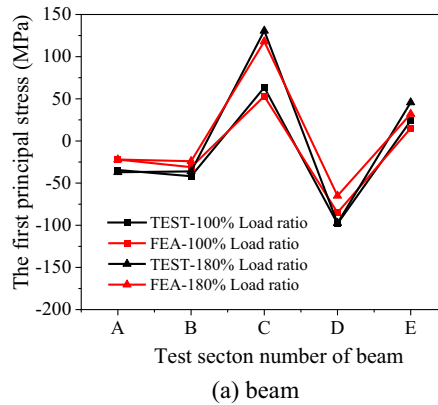
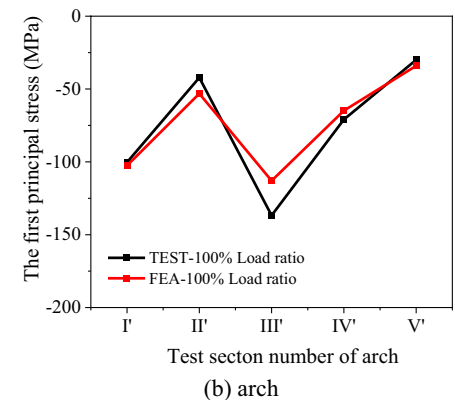
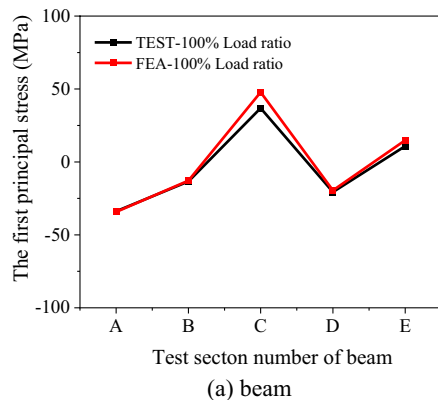


Fig. 14 The maximum principal stress curve on the W-2 specimen



4 Bucking analysis and optimal design

The beam–arch joint test failed due to the local buckling of the steel plate, highlighting the importance of addressing buckling problems in steel structure bridges. Therefore, to further study the buckling problem of tied arch bridges, the following will be analyzed in detail from two aspects: in-plane buckling and out-of-plane buckling.

4.1 Out-plane buckling analysis

Yuehu Bridge is a single-arch rib bridge, making buckling analysis an essential aspect of the bridge design process. The primary objective of this section is to investigate the stability of the arch rib, which serves as the main compression member of the arch bridge. Stability analysis involves addressing the eigenvalue problem and the structural members' large deformation problem, which are linear buckling and nonlinear buckling, respectively. The impact of critical parameters, such as the rise-to-span ratio and the angle of the arch footing, on the bridge structure's buckling will be studied. Linear buckling will then be considered for comparison with nonlinear buckling.

Only the dead load discussed is considered in the buckling analysis since the initial load, such as the prestressed hanger, is not magnified on the scale. Table 5 lists the buckling mode

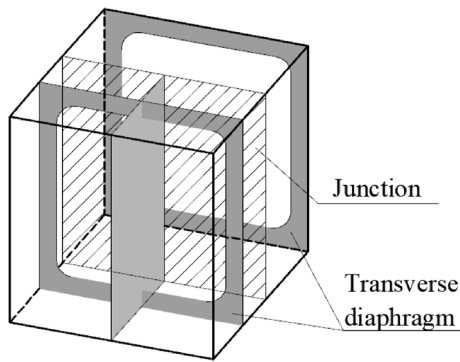


Fig. 15. The structure of the change of the chamber

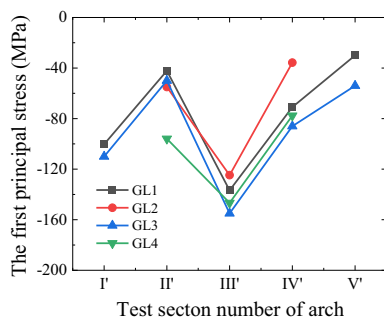
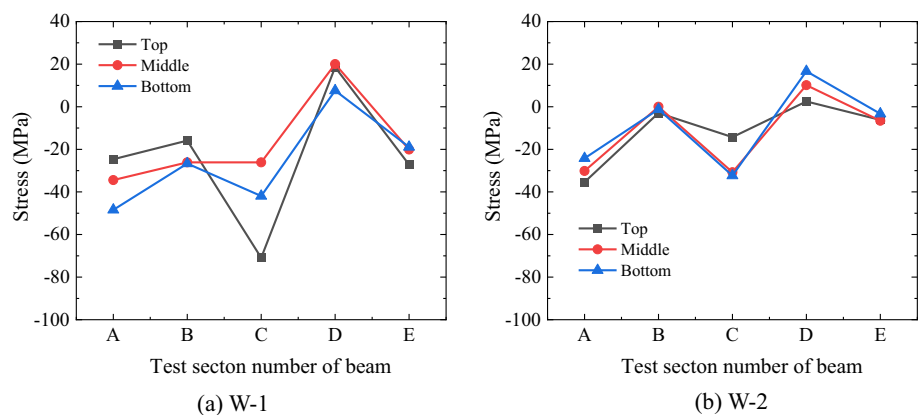


Fig. 16 The principal stress distribution on arch rib

shapes and the stability safety factors, which represent the fundamental frequencies and the instability mode, respectively. Since the design code for beam–arch bridges does not specify a stability safety factor, the relevant code for urban pedestrian overcrossing is used in engineering design. The lowest stability safety factors, which are larger than the requirement stipulated in CJJ 69-1995 [19], can be found in Table 5. Additionally, the first unstable mode is out-plane buckling, indicating that the out-plane stiffness of the arch bridge is less than the in-plane stiffness.

Fig. 17 Principal stress distribution on beam



To clarify the difference between the nonlinear and linear models, three kinds of nonlinear models were used to investigate the buckling analysis of the arch bridge. These models include Model-I (considering the geometric nonlinearity), Model II (considering the material nonlinearity), and Model III (considering both geometric and material nonlinearity).

There are three materials have been used, which are steel, steel wires, and concrete, respectively. The mechanical properties of materials are listed in Table 6.

Table 7 lists the stability safety factors of the three kinds of models. The stability safety factor values of nonlinear buckling models are notably less than those of the linear buckling analyses. Compared to the elastic linear model, the safety factor increments in the three models are – 23%, – 37%, and – 52%, respectively. However, even though Model III considers both nonlinearities, its safety factor is still larger than the smallest value required for a cable-stayed bridge (1.0) simultaneously. Therefore, the out-of-plane stiffness and stability of the arch bridge can meet the requirement.

For further analysis, the stiffness of the out-plane, the width-to-span ratio, and the rise-to-span ratio are considered. In Fig. 18, f , L , and B are the height of the arch, span length, and bridge width, respectively.

The effect of the width-to-span ratios on the stability safety factor is illustrated in Fig. 19. It can be observed that the stability safety factors significantly decrease as the width-to-span ratio increases. This is because the width-to-span ratio (B/L) reduces the arch bridge’s rigidity. Therefore, the bridge width can only be increased if the bridge’s stiffness is improved.

Another critical parameter in the design process of arch bridges is the rise-to-span ratio, which has a direct impact on the arch structure's static and dynamic characteristics. Figure 20 demonstrates that the stability safety factor is optimal as the rise-to-span ratio increases from 2.0 to 3.0.

Table 5 Stability safety factors and buckling mode shapes of the beam–arch bridge

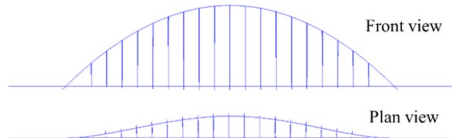
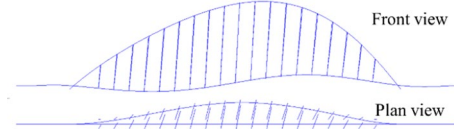
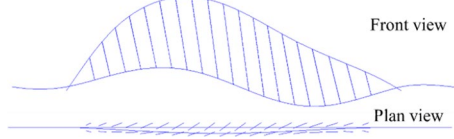
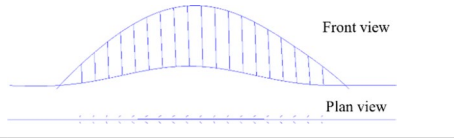
Order	Safety factor λ	Buckling mode shapes
1	4.63	
2	5.71	
3	5.80	
4	6.93	

Table 6 Mechanical properties of materials

Materials	Young’s modulus E	Poisson’s ratio ν	Yield stress σ
Steel	210 GPa	0.3	345 MPa
Steel wires	210 GPa	0.3	1860 MPa,
Concrete	35 GPa	0.2	50 MPa

Table 7 Safety factors of different models

Model	Safety factor λ	Increments
Elastic linear	4.63	–
Geometric nonlinear	3.56	– 23%
Inelastic nonlinear	2.94	– 37%
Both nonlinearities	2.21	– 52%

4.2 In-plane buckling analysis

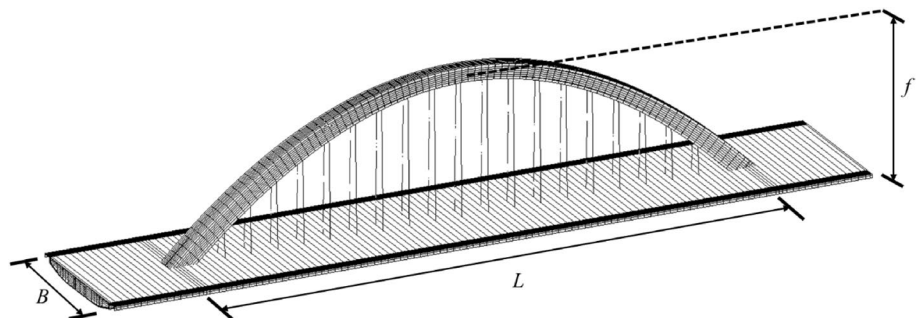
Pin-ended and fixed arches at two ends are considered in this paper, as shown in Fig. 21, in which f , L , S , and q denote the height of the arch, span, and length, and the uniformly distributed load, respectively.

The arch sections of the structures are doubly symmetric welded box sections. The value of the rise-to-span ratio f/L in this study is from 0.1 to 0.4. The in-plane slenderness of the arch λ_x is expressed as follows [20]:

$$\lambda_x = \begin{cases} 0.5S/i_x, & \text{the pin - ended arches} \\ 0.35S/i_x, & \text{arch fixed at two ends} \end{cases} \quad (1)$$

where μ = the effective length factor; and i_x = radius of gyration of the cross-section.

Fig. 18 Key parameters of the arch bridge



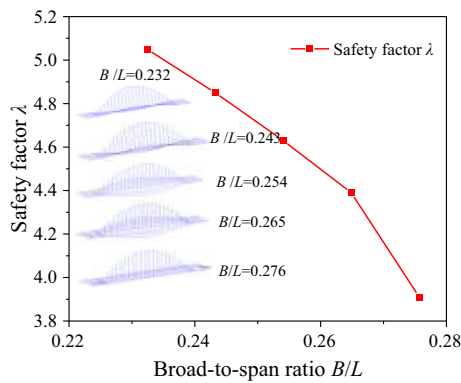


Fig. 19 Effect of the width-to-span ratio (B/L) on the safety factor

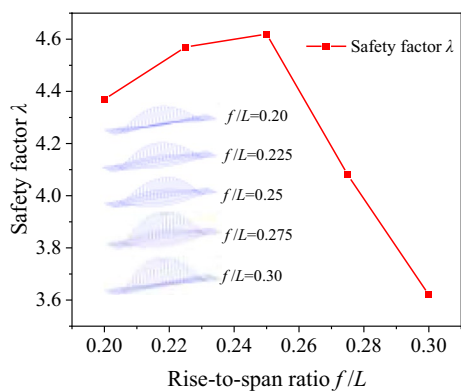


Fig. 20 Effect of the rise-to-span ratio (f/L) on the safety factor

The process of solving dynamic structural characteristics by finite element method is as follows.

Firstly, the in-plane buckling analysis was performed, and the buckling mode was extracted. Secondly, the initial geometric deformations were added to the prototype structure. Thirdly, the elastic–plastic deformation of the arch rib and ultimate strength values of the corresponding were tracked using the Newton–Raphson iterative method.

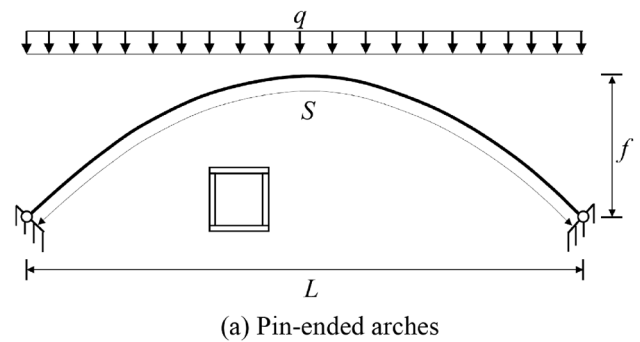
The strength of arches should be reduced under uniform compression, which is expressed as follow:

$$\varphi = N_u / N_y, \tag{2}$$

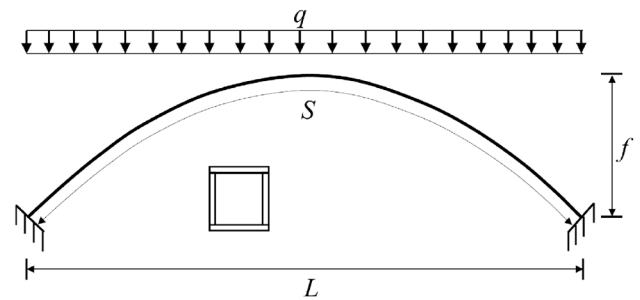
where N_u = the ultimate axial buckling strength; N_y = the squash load of the cross-section.

Geometric and material nonlinearities were taken into account in the analysis, and the stress–strain relationship of the material was bilinear, with the material yield strength being $1/50 E$, according to the code [21].

As shown in Fig. 22, initial imperfections have a significant impact on arches with different structures. The size of the box section is $h \times b \times t = 6000 \text{ mm} \times 6000 \text{ mm} \times 24 \text{ mm}$, and the rise-to-span ratio f/L is 0.25. According to the first-order



(a) Pin-ended arches



(b) Arch fixed at two ends

Fig. 21 Arches under uniformly distributed load

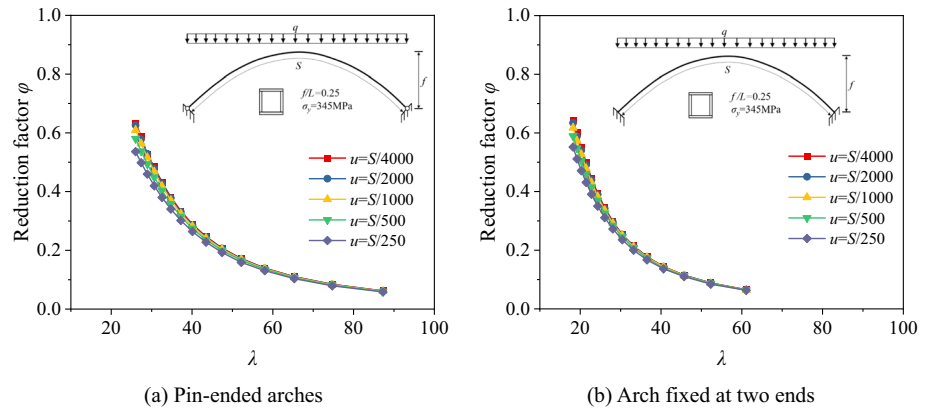
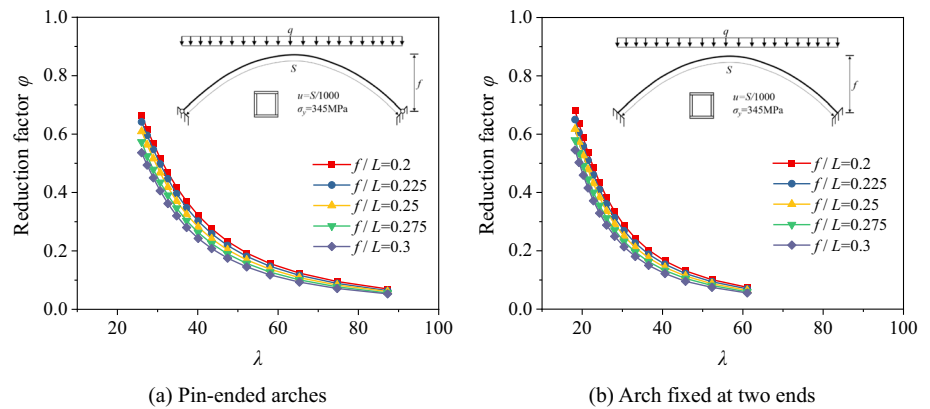
in-plane buckling mode analysis, the selected geometric imperfections are $S/4000$, $S/2000$, $S/1000$, $S/500$, and $S/250$, respectively.

The magnitude of the buckling strength is significantly related to geometric imperfections, and the reduction factors decrease remarkably as the geometric imperfections increase. However, geometric imperfections have little effect when the slenderness of the pin-ended arches and arch fixed at two ends is larger than 60 and 40, respectively. Comparing the effect of geometric imperfections on different structures, the lower reduction factor is observed for arch fixed at two ends arch bridges with the same λ .

The rise-to-span ratio is another critical parameter that affects the in-plane buckling strength of arches. Figure 23 shows two different structures that were analyzed to investigate the impact of the rise-to-span ratios. The results showed that the decrease in the rise-to-span ratio significantly impacted the buckling strength of the arches, both for pin-ended and arches fixed at two ends.

5 Conclusions

This paper analyzed the mechanical behavior of beam–arch bridges using experimental and finite element methods, focusing on the out-of-plane and in-plane buckling

Fig. 22 Effects of initial imperfections**Fig. 23** Effects of rise-to-span

strengths. The simulated results showed good agreement with the experimental results, enabling the following conclusions to be drawn:

1. The maximum stresses of the test model under 100% of the worst-case loading were less than the yield strength, which were 63 MPa and 194 MPa, respectively. This indicates that the beam–arch joint design is safe and rational for worst-case loads.
2. The model test results and finite element analysis results were in good agreement, with differences between experimental and simulated results mostly within 20%. The study demonstrated that finite element analysis is a reliable method for predicting the complex stress distribution in the design process of beam–arch joints. Moreover, FEA has higher economic efficiency than experimental analysis, making it necessary to promote its application in the design process.
3. The beam–arch bridge has good stability in both out-plane and in-plane buckling analysis. The rise-to-span ratio significantly affects the out-of-plane and in-plane buckling strength of arches. Besides, the width-to-span

ratio and initial imperfections also affect the buckling strength.

Overall, this study provides insights into the mechanical behavior of beam–arch bridges and highlights the importance of accurate design methods and reliable analysis techniques for ensuring the safety and reliability of such structures. The findings can guide the development of improved design methods and provide a basis for further research in this field.

Acknowledgements The work described in this paper is supported by grants from the Natural Science Foundation of Fujian Province (no. 2021J011062).

Data availability Data will be made available on request.

Declarations

Conflict of interest All authors confirm that they have no conflicts of interest.

Ethical approval All authors approve that the research was performed under all the ethical norms.

Consent to publish All authors consent to publish this paper.

Consent to participate Not applicable.

References

1. Bayraktar A, Türker T, Altunişik AC. Experimental frequencies and damping ratios for historical masonry arch bridges. *Constr Build Mater*. 2015;75:234–41. <https://doi.org/10.1016/j.conbuildmat.2014.10.044>.
2. Kang HJ, Zhao YY, Zhu HP, Jin YX. Static behavior of a new type of cable-arch bridge. *J Constr Steel Res*. 2013;81:1–10. <https://doi.org/10.1016/j.jcsr.2012.10.010>.
3. Ma H, Zheng H, Zhang W, Tang Z, Lui EM. Experimental and numerical study of mechanical behavior of welded steel plate joints. *Metals*. 2020;10:1293. <https://doi.org/10.3390/met10101293>.
4. Ye M, Huang Q, Wu Q. Analysis of steel-concrete composite structure with overlap slab of Xingguang bridge. *J Cent South Univ Technol*. 2007;14:120–4. <https://doi.org/10.1007/s11771-007-0024-1>.
5. Huynh CP, Mustapha S, Runcie P, Porikli F. Multi-class support vector machines for paint condition assessment on the Sydney Harbour Bridge using hyperspectral imaging. *Struct Monit Maint*. 2015;2:181–97. <https://doi.org/10.12989/smm.2015.2.3.181>.
6. Fan B, Wang S, Chen B. Dynamic effect of tie-bar failure on through tied arch bridge. *J Perform Constr Facil*. 2020;34:04020089. [https://doi.org/10.1061/\(ASCE\)CF.1943-5509.0001492](https://doi.org/10.1061/(ASCE)CF.1943-5509.0001492).
7. Feng Y. Research and scale model test on the local stability of steel box arch segment of Lupu Bridge. In: Shen ZY, Li GQ, Chan SL, editors. Fourth international conference on advances in steel structure. Oxford: Elsevier Science Ltd; 2005. p. 1663–7. <https://doi.org/10.1016/B978-008044637-0/50248-1>.
8. Zhang K-B, Zhang J-R, Yan D-H. Model test of half-through CFST tied-arch bridge in the process of arch rib erection. *Struct Eng Int*. 2008;18:396–402. <https://doi.org/10.2749/101686608786455199>.
9. Liu A-R, Huang Y-H, Fu J-Y, Yu Q-C, Rao R. Experimental research on stable ultimate bearing capacity of leaning-type arch rib systems. *J Constr Steel Res*. 2015;114:281–92. <https://doi.org/10.1016/j.jcsr.2015.08.011>.
10. La Poutré DB, Spooenberg RC, Snijder HH, Hoenderkamp JCD. Out-of-plane stability of roller bent steel arches—an experimental investigation. *J Constr Steel Res*. 2013;81:20–34. <https://doi.org/10.1016/j.jcsr.2012.11.004>.
11. Wei J, Wu Q, Chen B, Wang T-L. Equivalent beam-column method to estimate in-plane critical loads of parabolic fixed steel arches. *J Bridge Eng*. 2009;14:346–54. [https://doi.org/10.1061/\(ASCE\)1084-0702\(2009\)14:5\(346\)](https://doi.org/10.1061/(ASCE)1084-0702(2009)14:5(346)).
12. Guo Y-L, Zhao S-Y, Pi Y-L, Bradford MA, Dou C. An experimental study on out-of-plane inelastic buckling strength of fixed steel arches. *Eng Struct*. 2015;98:118–27. <https://doi.org/10.1016/j.engstruct.2015.04.029>.
13. Lu Y, Cheng Y, Han Q. Experimental investigation into the in-plane buckling and ultimate resistance of circular steel arches with elastic horizontal and rotational end restraints. *Thin-Walled Struct*. 2017;118:164–80. <https://doi.org/10.1016/j.tws.2017.05.010>.
14. Huang Y, Liu A, Zhu C, Lu H, Gao W. Experimental and numerical investigations on out-of-plane ultimate resistance of parallel twin-arch under uniform radial load. *Thin-Walled Struct*. 2019;135:147–59. <https://doi.org/10.1016/j.tws.2018.10.042>.
15. Laterza M, et al. Stress-life curves method for fatigue assessment of ancient brick arch bridges. *Int J Archit Herit*. 2017;11(6):843–58. <https://doi.org/10.1080/15583058.2017.1315621>.
16. Casamassima VM, D'Amato M. Fatigue assessment and deterioration effects on masonry elements: a review of numerical models and their application to a case study. *Front Built Environ*. 2019;5(65):1–10. <https://doi.org/10.3389/fbuil.2019.00065>.
17. D'Amato M, et al. Seismic performance evaluation of a multi-span existing masonry arch bridge. *Open Civ Eng J*. 2017;11(11):1191–207. <https://doi.org/10.2174/1874149501711011191>.
18. Ministry of housing and urban-rural development of China. Standard for design of steel structures. Beijing: GB 50017 Architecture and Building Press; 2017.
19. Industry Standard of the People's Republic of China. Technical specifications of urban pedestrian overcrossing and underpass. Beijing: CJJ 69-1995 China Architecture and Building Press. 1996.
20. Pi YL, Nicholas ST. In-plane inelastic buckling and strengths of steel arches. *J Struct Eng*. 1996;122(7):734–47.
21. Ministry of housing and urban-rural development of China. Technical specification for steel arch structure. Beijing: JGJ/T 249 Architecture and Building Press; 2011.

Publisher's Note Springer Nature remains neutral with regard to jurisdictional claims in published maps and institutional affiliations.

Springer Nature or its licensor (e.g. a society or other partner) holds exclusive rights to this article under a publishing agreement with the author(s) or other rightsholder(s); author self-archiving of the accepted manuscript version of this article is solely governed by the terms of such publishing agreement and applicable law.